

See discussions, stats, and author profiles for this publication at: <http://www.researchgate.net/publication/272171883>

# The Role of the Inner Coronal Null Point in the Formation and Evolution of Solar Quiescent Prominences

ARTICLE *in* THE ASTROPHYSICAL JOURNAL · MARCH 2015

Impact Factor: 6.28 · DOI: 10.1088/0004-637X/800/1/43

---

DOWNLOADS

21

---

VIEWS

33

1 AUTHOR:



[Y. Z. Zhang](#)

National Space Science

9 PUBLICATIONS 57 CITATIONS

SEE PROFILE

# THE ROLE OF THE INNER CORONAL NULL POINT IN THE FORMATION AND EVOLUTION OF SOLAR QUIESCENT PROMINENCES

Y. Z. ZHANG

State Key Laboratory for Space Weather, Center for Space Science and Applied Research, Chinese Academy of Sciences,  
 Beijing 100080, China; yzzhangmail@sohu.com

Received 2014 July 15; accepted 2014 December 10; published 2015 February 6

## ABSTRACT

Using a 2.5-dimensional MHD simulation, we investigate the role played by the inner coronal null point in the formation and evolution of solar quiescent prominences. The flux rope is characterized by its magnetic fluxes, the toroidal magnetic flux  $\Phi_p$  and the poloidal flux  $\Phi_\varphi$ . It is found that for a given  $\Phi_p$ , the catastrophe does not occur in the flux rope system until  $\Phi_\varphi$  increases to a critical point. Moreover, the magnetic flux of the null point is the maximum value of the magnetic flux in the quadrupole background magnetic field, and represented by  $\psi_N$ . The results show that the bigger  $\psi_N$  usually corresponds to the smaller catastrophic point, the lower magnetic energy of the flux rope system, and the lesser magnetic energy inside the flux rope. Our results confirm that catastrophic disruption of the prominence occurs more easily when there is a bigger  $\psi_N$ . However,  $\psi_N$  has little influence on the maximum speed of the coronal mass ejections (CMEs) with an erupted prominence. Thus we argue that a topological configuration with the inner coronal null point is a necessary structure for the formation and evolution of solar quiescent prominences. In conclusion, it is easier for the prominences to form and to erupt as a core part of the CMEs in the magnetic structure with a greater  $\psi_N$ .

**Key words:** Sun: corona – Sun: coronal mass ejections (CMEs) – Sun: filaments, prominences

## 1. INTRODUCTION

The formation and evolution of solar quiescent prominences (or filaments) is an important unsolved problem in solar physics. At present, it is widely accepted that the magnetic field plays an important role in the filament eruption process. The original model for solar prominences relied on dips in the magnetic to hold the cool plasma against gravity (e.g., Kippenhahn & Schlüter 1957; Hyder 1967; Kuperus & Raadu 1974; Heyvaerts et al. 1977; Spicer 1977; Milne et al. 1979; Anzer & Priest 1985; Zirker 1989; Antiochos et al. 1994; Forbes et al. 1994; Low & Hundhausen 1995; Tandberg-Hanssen 1995; Aulanier & Demoulin 1998; Martin 1998; Heinzel & Anzer 1999; Labrosse et al. 2010; Mackay et al. 2010; Low et al. 2012). This classic model has been extended in three ways to account for energy storage and release. The first considers magnetic reconnection in the extended current sheet and on the tearing mode instability by magnetic shear in the dynamics of prominences (e.g., Foukal & Behr 1995; DeVore & Antiochos 2000; Petrie & Low 2005; Welsch et al. 2005; Luna et al. 2012; Xia et al. 2012). The second uses the cancelation of converging magnetic flux (e.g., Galsgaard & Longbottom 1999; Martens & Zwaan 2001; Litvinenko & Wheatland 2005; López et al. 2006; Mackay & van Ballegooijen 2006a, 2006b; Litvinenko et al. 2007). The third relies on the emergence of a magnetic flux rope (e.g., Low & Zhang 2002; Fong et al. 2002; Aulanier & Demoulin 2003; Low & Petrie 2005; Okamoto et al. 2009; Magara 2012; Hillier & van Ballegooijen 2013; Zhang 2013; Longcope & Forbes 2014; Kliem et al. 2014). In this work, we discuss the dynamical evolution of a flux rope system in a complicated background field.

Observations show that the prominences are usually suspended in the inner corona within a magnetic complex consisting of regions (e.g., Newkirk 1967; Saito & Hyder 1968; Bohlin 1970; Waldmeier 1970; Pneuman 1972; Saito & Tandberg-Hanssen 1973; Webb et al. 1976; Schmahl & Hildner 1977; Serio et al. 1978; Dryer 1982; MacQueen et al. 1983; Illing

1984; Athay & Illing 1986; Illing & Hundhausen 1986; Gopalswamy & Kundu 1990; Raju et al. 1993; Gopalswamy et al. 1997; Wiik et al. 1994; Low 2001; Marqué 2004; Koutchmy et al. 2004; Gibson et al. 2006, 2010; Wang et al. 2006; Zhou et al. 2006a, 2006b; Heinzel et al. 2008; Zhang & Li 2009; Habbal et al. 2010; Su et al. 2010; Li et al. 2011; Régnier et al. 2011; Berger et al. 2012; Vourlidis et al. 2013; Parenti 2014; Yang et al. 2014). Introducing the quadrupole field to flux rope catastrophe model, we found that there are two current sheets in the flux rope system, one is a vertical current sheet connected to the solar surface and the flux rope, and the other is a transversal sheet evolved from the null point, which was originally located in the inner corona (Zhang et al. 2005; Zhang & Wang 2007). Furthermore, the recent paper presented by Zhang (2013) shows that after the first catastrophe the quiescent prominences are supported by the vertical and transverse current sheets in the inner corona, and after the second catastrophe the prominence would erupt as a part of coronal mass ejections (CMEs). The magnetic null point is an important part of the magnetic field structure, and it is essential to the formation of the current sheet. Therefore, the purpose of this paper is to study the role of the inner corona null point in the formation and eruption of quiescent prominences using a magnetic flux rope catastrophe model. The model is introduced in Section 2, and the numerical results are discussed in Section 3. Finally, in Section 4, we discuss several conclusions.

## 2. NUMERICAL MODEL

Using time-dependent resistive MHD simulations, we study the evolution of solar quiescent prominences. For 2.5-dimensional MHD problems in spherical coordinates  $(r, \theta, \varphi)$ , a magnetic flux function  $\psi(t, r, \theta)$  was introduced, and it is related to the magnetic field by

$$\mathbf{B} = \nabla \times \left( \frac{\psi}{r \sin \theta} \hat{\varphi} \right) + \mathbf{B}_\varphi, \quad \mathbf{B}_\varphi = B_\varphi \hat{\varphi}, \quad (1)$$

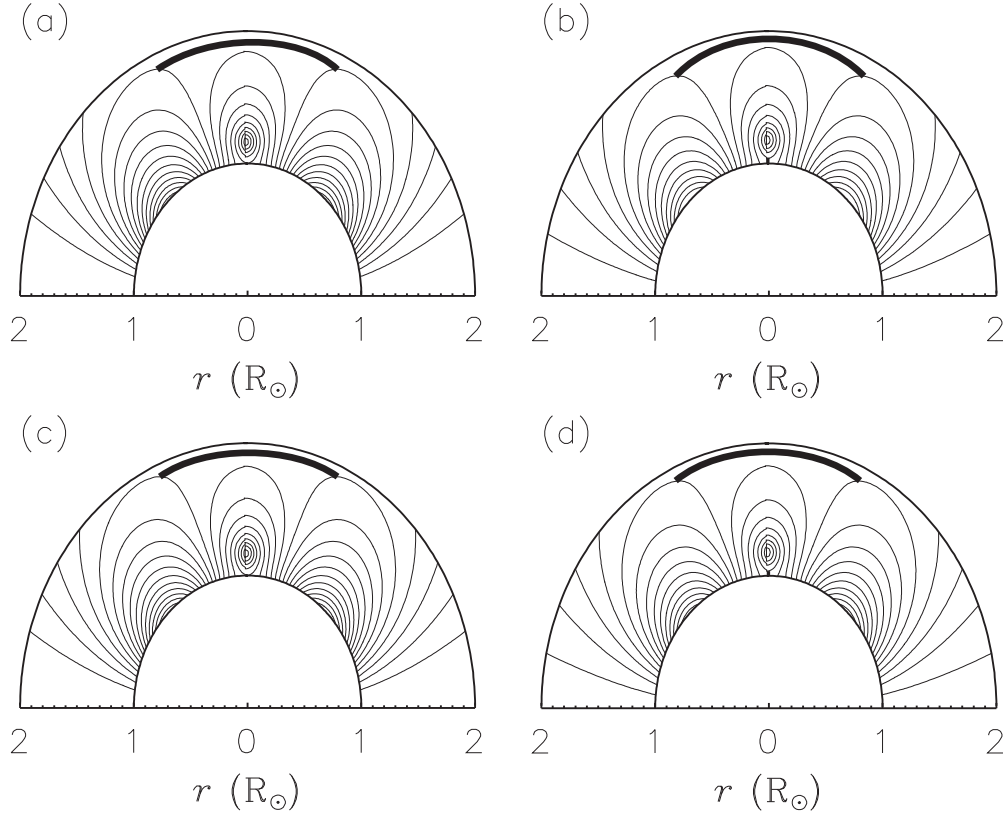


**Figure 1.** Magnetic configurations of the flux rope system corresponding to two cases: for case A,  $\alpha = 1.0$ ,  $\Phi_p = 0.36$  and two separate values of  $\Phi_\phi$ : (a) 0.0621 right before and (b) 0.0622 right after the first catastrophic point. For case B,  $\alpha = 1.01$ ,  $\Phi_p = 0.36$  and two separate values of  $\Phi_\phi$ : (c) 0.0641 right before and (d) 0.0642 right after the first catastrophic point. The outline of the electric current sheets is depicted by thick solid curves.

where  $B_\phi$  is the azimuthal component of the magnetic field. Then the corresponding resistive MHD equations are cast in the following form:

$$\frac{\partial \rho}{\partial t} + \nabla \cdot (\rho \mathbf{v}) = 0, \quad (2)$$

$$\frac{\partial \mathbf{v}}{\partial t} + \mathbf{v} \cdot \nabla \mathbf{v} + \frac{1}{\rho} \nabla p + \frac{1}{\mu \rho} [L\psi \nabla \psi + \mathbf{B}_\phi \times (\nabla \times \mathbf{B}_\phi)] + \frac{1}{\mu \rho r \sin \theta} \nabla \psi \cdot (\nabla \times \mathbf{B}_\phi) \hat{\phi} + \frac{GM_\odot}{r^2} \hat{r} = 0, \quad (3)$$

$$\frac{\partial \psi}{\partial t} + \mathbf{v} \cdot \nabla \psi - \frac{1}{\mu} \eta r^2 \sin^2 \theta L\psi = 0, \quad (4)$$

$$\begin{aligned} \frac{\partial B_\phi}{\partial t} + r \sin \theta \nabla \cdot \left( \frac{B_\phi \mathbf{v}}{r \sin \theta} \right) + \left[ \nabla \psi \times \nabla \left( \frac{v_\phi}{r \sin \theta} \right) \right]_\phi \\ - \frac{1}{r \sin \theta} \nabla \eta \cdot \nabla (\mu r \sin \theta B_\phi) \\ - \frac{1}{\mu} \eta r \sin \theta L(r B_\phi \sin \theta) = 0, \end{aligned} \quad (5)$$

$$\frac{\partial T}{\partial t} + \mathbf{v} \cdot \nabla T + (\gamma - 1) T \nabla \cdot \mathbf{v} - \frac{\gamma - 1}{\rho} \eta \mathbf{j}^2 = 0, \quad (6)$$

where

$$L\psi \equiv \frac{1}{r^2 \sin^2 \theta} \left( \frac{\partial^2 \psi}{\partial r^2} + \frac{1}{r^2} \frac{\partial^2 \psi}{\partial \theta^2} - \frac{\cot \theta}{r^2} \frac{\partial \psi}{\partial \theta} \right), \quad (7)$$

$$\mathbf{j} = \frac{1}{\mu} \nabla \times \mathbf{B} = -\frac{1}{\mu} r \sin \theta L\psi \hat{\phi} + \frac{1}{\mu} \nabla \times (B_\phi \hat{\phi}), \quad (8)$$

$\gamma (= 1.05)$  is the polytropic index,  $\eta$  is the resistivity, and  $\mathbf{j}$  is the current density. The solution domain is taken to be  $1 \leq r \leq 30$ ,  $0 \leq \theta \leq \pi/2$ , discretized into  $130 \times 90$  grid points. The MHD equations are solved with the multi-step implicit scheme developed by Hu (1989).

The initial quiet corona is assumed to be isothermal and static with  $T_0 = 1.4 \times 10^6$  K and  $\rho_0 = 6.68 \times 10^{-13}$  kg m $^{-3}$  at the coronal base. The ratio of gas pressure to magnetic pressure is  $\beta = 0.03$ , and then the unit of  $\psi$  is  $\psi_0 = (2\mu\rho_0 RT_0 R_s^4/\beta)^{1/2} = 5.50 \times 10^{14}$  Wb, the unit of magnetic field intensity is  $B_0 = \psi_0/R_s^2 = 1.14 \times 10^{-3}$  T,  $v_A = B_0/(\mu\rho_0)^{1/2} = 1242$  km s $^{-1}$  for velocity,  $\tau_A = R_s/v_A = 560$  s for time, the unit of magnetic energy is  $E_0 = B_0^2 R_s^3/\mu = 3.47 \times 10^{26}$  J, and  $j_0 = B_0/(\mu R_\odot) = 1.31 \times 10^{-6}$  A m $^{-2}$  for current density.

The initial background magnetic field is a quadrupole field (Antiochos et al. 1999; Hu 2004; Zhang et al. 2005; Zhang 2013), and the related magnetic flux function normalized by  $\psi_0$  is given by

$$\psi(r, \theta) = \frac{\sin^2 \theta}{r} + \frac{\alpha(3 + 5 \cos 2\theta) \sin^2 \theta}{2r^3}, \quad (9)$$

where  $r$  is in units of  $R_s$ , and  $\alpha$  is the control parameter of magnetic flux. Moreover, the magnetic flux of the null point is the maximum value of magnetic flux in the quadrupole background magnetic field, and is represented by  $\psi_N$ . During a magnetic flux rope emerging from the bottom of the corona into the central arcade, the null point evolves into the transverse current sheet.

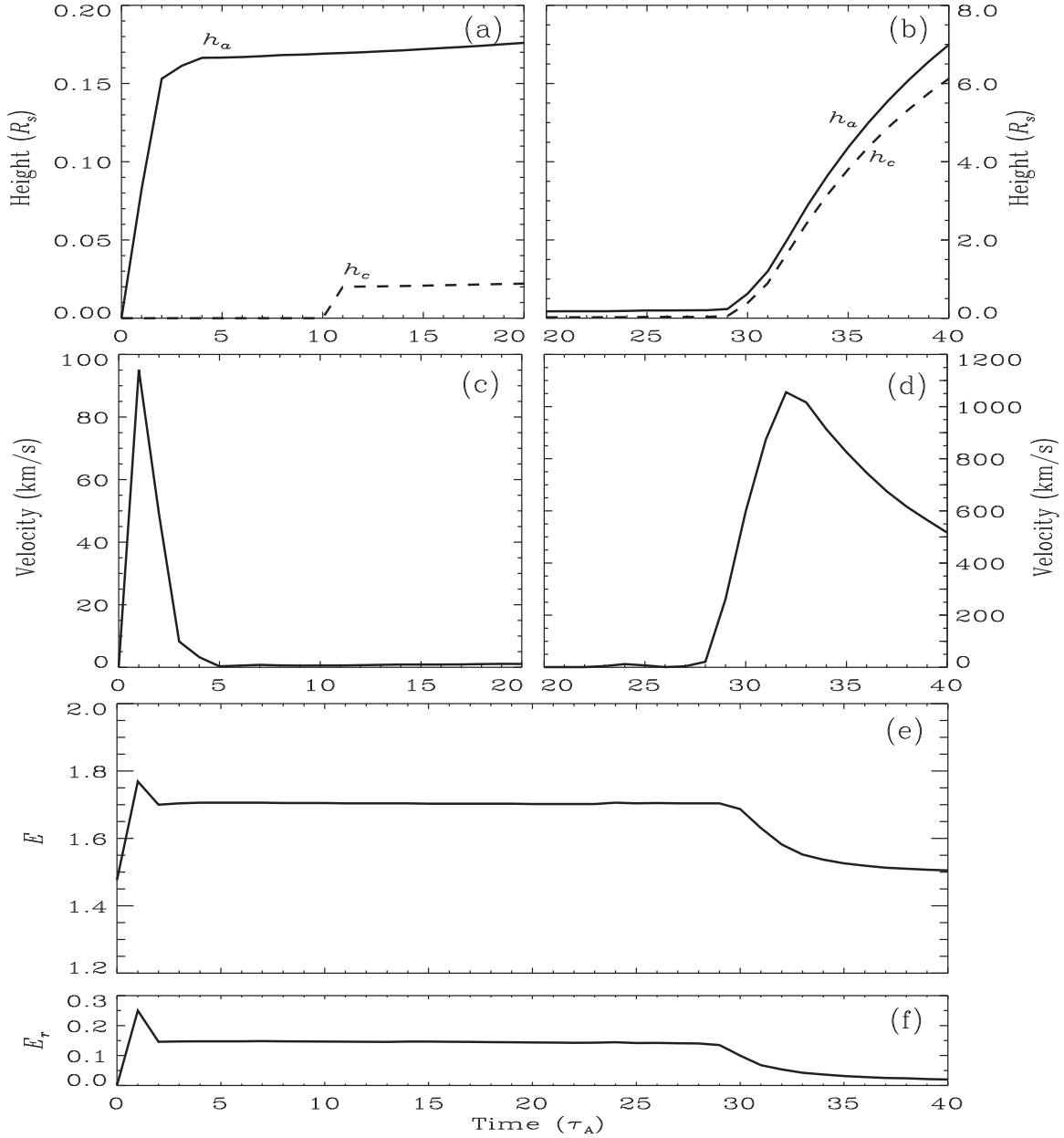


**Figure 2.** For case A: heights of the coronal magnetic flux rope vs. time (panels (a) and (b)), velocity of the flux rope axis vs. time (panels (c) and (d)), and magnetic energy of the system and of the flux rope vs. time (panels (e) and (f)).

Furthermore, we calculate the magnetic energy  $E$  of the force-free field, normalized by  $4\pi E_0$ , using

$$E = \frac{1}{2} \int_1^{30} dr \int_0^{\pi/2} B^2 r^2 \sin \theta d\theta + \frac{30^3}{2} \int_0^{\pi/2} (B_r^2 - B_\theta^2)_{r=30} \sin \theta d\theta, \quad (10)$$

where the first term on the right-hand side is the magnetic energy in the computational domain ( $1 \leq r \leq 30$ ;  $0 \leq \theta \leq \pi$ ;  $0 \leq \varphi \leq 2\pi$ ) and the second is that outside of the domain, having been transformed into a surface integral over the top (Hu 2004). In addition, magnetic energy inside the flux rope,  $E_r$ , is obtained by an integral representation similar to the first term on the right-hand side of the Equation (10), but with the integral domain limited to the interior of the rope ( $\psi < 0$ ).

Zhang (2013) shows that the formation of solar quiescent prominences may well be an ideal MHD process, and the prominences are supported by the vertical current sheet and located in cavities below the curved transverse current sheet in the inner corona after the first catastrophe. However, in the process of prominence eruption, magnetic reconnection occurs in the vertical and transverse current sheets after the second catastrophe. Moreover, we introduce a critical current density for the two current sheets, the vertical one is  $j_v = 20$  and the transverse one is  $j_t = 5$  (see Zhang & Wang 2007). Besides, we choose the critical length of the vertical current sheet,  $l_c = 0.5 R_\odot$ , which is large enough to satisfy the tearing mode instability (Furth et al. 1963). Therefore, the current density nearby the transverse current sheet exceeds  $j_t$ , or that nearby the vertical current sheet exceeds  $j_v$  and the length of the vertical current sheet also exceeds  $l_c$ ;  $\eta$  is set to 0.01, and  $\eta$  is set to zero elsewhere (Zhang et al. 2006). In the present study, the flux rope

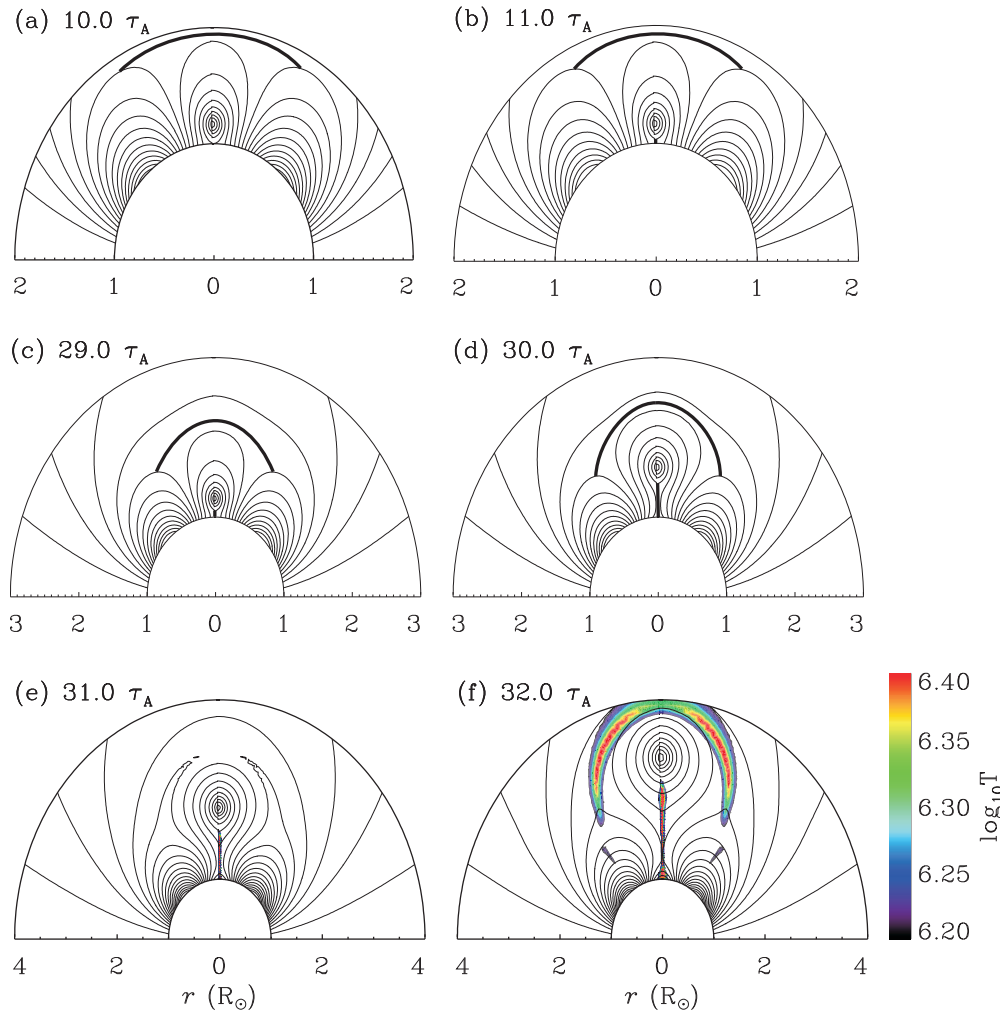


**Figure 3.** Magnetic configuration in black solid curves and temperature distribution in color at several separate times for case A, in which just before and after the first catastrophe (panels (a) and (b)), just before and after the second catastrophe (panels (c) and (d)), reconnection occurs in the vertical and transverse current sheets (panel (e)), and then the velocity of the CMEs reaches the maximum speed (panel (f)). The cool blue and hot red correspond to  $1.58 \times 10^6$  and  $2.51 \times 10^6$  K, respectively.

is characterized by the toroidal magnetic flux  $\Phi_p$  and poloidal flux  $\Phi_\phi$ . First, in the ideal MHD simulation, it is found that for a given  $\Phi_p$ , the catastrophe does not occur in the flux rope system until  $\Phi_\phi$  increases to a critical point.  $\Phi_\phi$  is the catastrophe point for  $\Phi_p$ . Then in the time-dependent resistive MHD simulation, the flux rope represented by the  $\Phi_p$  and the  $\Phi_\phi$  has emerged from the bottom of corona into the central arcade. The evolution of the flux rope system shows that after the first catastrophe the prominences are formed in the inner corona, and after a period of time the second catastrophe occurs, meanwhile, the prominences erupt as a main part of CMEs that resulted in the magnetic reconnection taking place in the two current sheets.

### 3. SIMULATION RESULTS

In our simulation, two parameters are used to describe the geometrical characteristics of the flux rope system in equilibrium. One is  $h_c$ , the length of the vertical current sheet, the other one is  $h_a$ , the height of the quiescent prominences (HQP). Moreover, the magnetic properties of the flux rope are represented by  $\Phi_p$ , the toroidal magnetic flux, and  $\Phi_\phi$ , the poloidal magnetic flux. In order to investigate the role of the inner coronal null point in the formation and evolution of quiescent prominences, two different  $\alpha$  are chosen: 1.0 and 1.01.

**Table 1**  
Magnetic Energies of the Flux Rope System and Magnetic Flux of the Maximum in the Magnetic Configuration,  $\psi_N$ , for Each  $\alpha$

$\alpha$	$\psi_N$	$E_0$
1.0	0.3849	1.476
1.01	0.3830	1.499

**Note.** See the text for details.

Then, we find two cases: case A and case B, respectively. When  $\alpha$  increases,  $\psi_N$  decreases, and the magnetic energy of the flux rope system  $E_0$  increases (see Table 1).

#### 3.1. Formation of Solar Quiescent Prominences

In the quadrupole magnetic field structure, quiescent prominences may be formed by the first catastrophe (Zhang 2013). In this simulation, with the same emerging strength of magnetic flux,  $\Phi_p = 0.36$ , we obtain two different catastrophic points,  $\Phi_\phi = 0.0622$  and  $0.0642$ , for which  $\alpha = 1.0$  and  $1.01$ , respectively. For case A, at  $\Phi_\phi = 0.0621$ , the flux rope sticks to the solar surface, and a curved transverse current sheet is formed above the flux rope (Figure 1(a)). Then at  $\Phi_\phi = 0.0622$ , the flux rope breaks away from the solar surface, and suspends stably

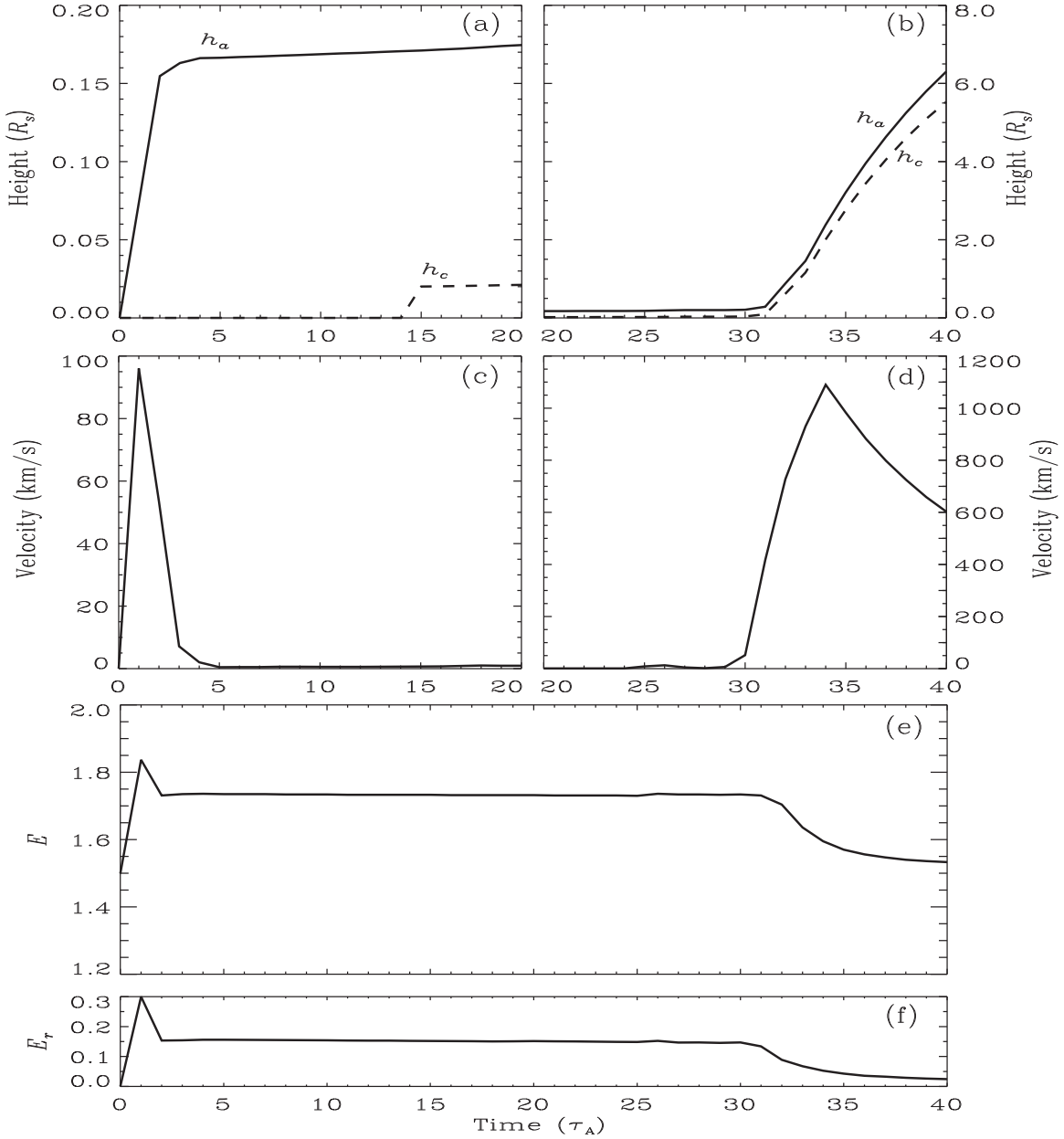


**Figure 4.** For case B: heights of the coronal magnetic flux rope vs. time (panels (a) and (b)), velocity of the flux rope axis vs. time (panels (c) and (d)), and magnetic energy of the system and of the flux rope vs. time (panels (e) and (f)).

in the inner corona, for which the flux rope is located above the short vertical current sheet and below the transverse current sheet (Figure 1(b)). Similarly, for case B, at  $\Phi_\varphi = 0.0641$ , there has been no catastrophe in the system (Figure 1(c)), and right at  $\Phi_\varphi = 0.0642$ , the first catastrophe occurs (Figure 1(d)). Furthermore, comparing case A and case B, we find that the bigger  $\psi_N$  corresponds to the smaller catastrophic point, the lower magnetic energy of the flux system, the lesser magnetic energy inside the flux rope, and the similar HQP (see Tables 2 and 3).

### 3.2. Evolution of Solar Quiescent Prominences

In the simulation, the magnetic flux rope represented by  $(\Phi_p, \Phi_\varphi)$  has emerged from the bottom of the corona into the central arcade, and we obtain the results of the evolution of flux rope system. With the purpose of studying the effect

**Table 2**  
Geometrical Characteristics and Magnetic Energies of the Flux Rope System Just Before and After the First Catastrophe for Case A, for which  $\alpha = 1.0$

$\Phi_p$	$\Phi_\varphi$	$h_c$ ( $R_s$ )	HQP ( $R_s$ )	$E$	$E_r$
0.36	0.0621	0.0	0.1656	1.709	0.1491
0.36	0.0622	0.02209	0.1780	1.713	0.1497

**Note.** See the text for details.

of  $\alpha$  on prominence evolution,  $(\Phi_p = 0.36, \Phi_\varphi = 0.0622)$  and  $(\Phi_p = 0.36, \Phi_\varphi = 0.0642)$  are chosen for case A and case B, respectively. Figure 2(a) shows that the flux rope has emerged into the arcade, and then the prominences are formed by the first catastrophe after  $\tau_A = 10$ . Both HQP and  $h_c$  rise

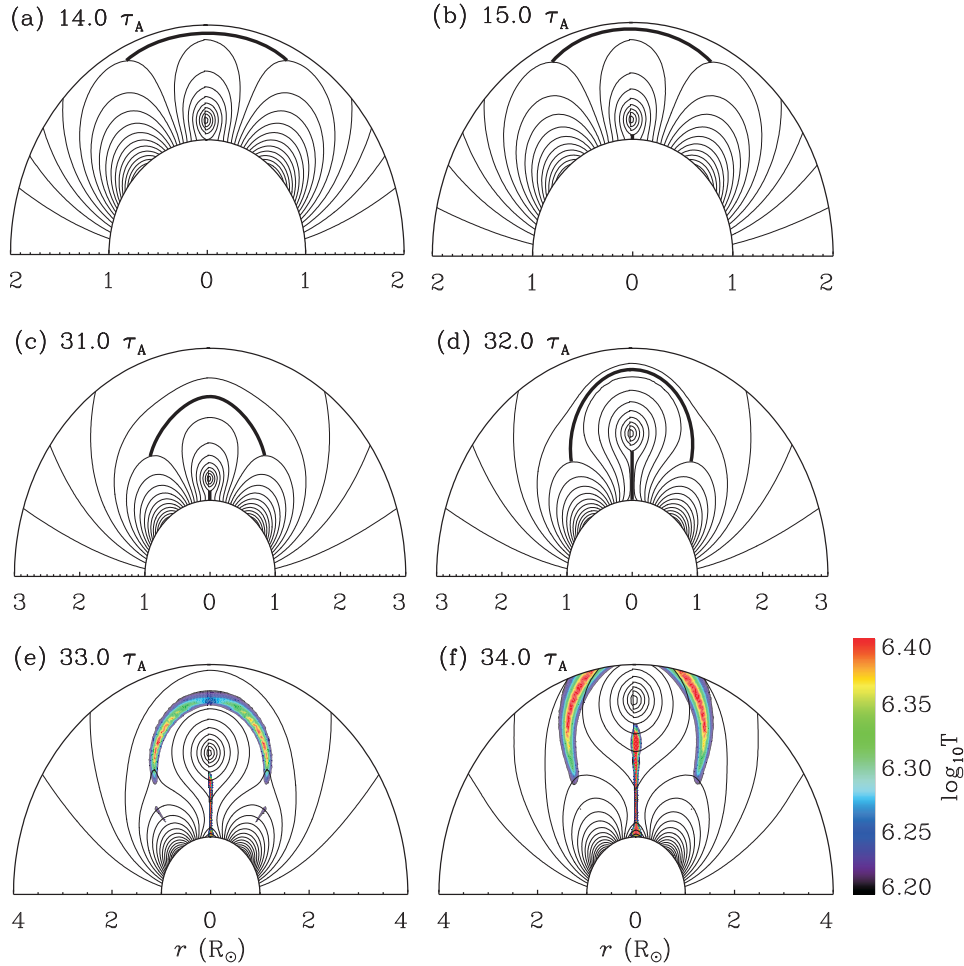


**Figure 5.** Magnetic configuration in black solid curves and temperature distribution in color at several separate times for case B, in which just before and after the first catastrophe (panels (a) and (b)), just before and after the second catastrophe (panels (c) and (d)), reconnection occurs simultaneously in the vertical and transverse current sheets (panel (e)), and then the velocity of the CMEs reaches the maximum speed (panel (f)). The cool blue and hot red correspond to  $1.58 \times 10^6$  and  $2.51 \times 10^6$  K, respectively.

**Table 3**

Geometrical Characteristics and Magnetic Energies of the Flux Rope System Just Before and After the First Catastrophe for Case B, for which  $\alpha = 1.01$

$\Phi_p$	$\Phi_\varphi$	$h_c$ ( $R_s$ )	HQP ( $R_s$ )	$E$	$E_r$
0.36	0.0641	0.0	0.1681	1.739	0.1577
0.36	0.0642	0.02171	0.1791	1.745	0.1575

**Note.** See the text for details.

slowly until the second catastrophe occurs. After  $\tau_A = 29$ , HQP increases from  $0.2345 R_s$  to  $0.6252 R_s$ , and  $h_c$  increases from  $0.05422 R_s$  to  $0.3881 R_s$ , respectively (Figure 2(b)). Because of the prominence eruption, HQP increases quickly. Figure 2(c) shows that the velocity of the flux rope was within the range of  $0.5 \text{ km s}^{-1}$  and  $1.5 \text{ km s}^{-1}$  before  $20\tau_A$  except that the velocity increased rapidly and then fell quickly before  $5\tau_A$ . Meanwhile, the velocity has no obvious change even though the first catastrophe occurs. Figure 2(d) shows that the prominences have an oscillation process before the second catastrophe, and then the prominences erupt to reach the maximum speed of  $1055 \text{ km s}^{-1}$  at  $32\tau_A$ . In the beginning of the emergence of the flux rope, the magnetic energy of the flux rope system increases from 1.476 to 1.769 in a very short period of time. However, soon afterward, the energy decreases to 1.704, and then it has

no change even though the first catastrophe occurs. Until the second catastrophe happens, it significantly decreases to 1.582 at which the prominences reach the maximum speed (Figure 2(e)). Furthermore, the variation curve of magnetic energy inside the flux rope is similar to that of the flux rope system (Figure 2(f)).

Figure 3 describes the evolution of magnetic flux rope system at several separate times for case A. Before  $t = 10\tau_A$ , the catastrophe does not occur for which the flux rope below the undeveloped transverse current sheet attaches to the solar surface (Figure 3(a)). At about  $t = 11\tau_A$ , the first catastrophe occurs, and the length of the vertical current sheet below the rope is  $0.02007 R_s$  (Figure 3(b)). The quiescent prominences have levitated in the inner corona until  $t = 29\tau_A$  (Figure 3(c)). Then, at about  $t = 30\tau_A$ , the second catastrophe occurs and the prominences erupt, namely, the CMEs onset. However, at this time, magnetic reconnection does not occur in the elongated vertical current sheet and the curved transverse current yet (Figure 3(d)). Obviously, Figure 3(e) shows that magnetic reconnection has just happened in the transverse current sheet while it has already occurred in the vertical current sheet. At about  $t = 32\tau_A$ , the velocity of the CMEs reaches the maximum speed, and the plasmas around the two current sheets are heated by reconnection (Figure 3(f)). Consequently, the prominences erupt as the main component of the three-part CMEs and are always accompanied by two-ribbon flares.



For case B, Figure 4(a) shows that the first catastrophe occurs at about  $t = 15\tau_A$ , and the length of the vertical current sheet below the flux rope is  $0.02009R_s$ . Figure 4(b) shows that the second catastrophe occurs after  $t = 31\tau_A$ , and then the prominences rapidly erupt into the interplanetary space. From  $5\tau_A$  to  $20\tau_A$ , the velocity of the rope has been within the range of  $0.5\text{ km s}^{-1}$  to  $1.0\text{ km s}^{-1}$  (Figure 4(c)). After a period of oscillation, the second catastrophe occurs, and then the prominences erupt and reach the maximum speed of  $1090\text{ km s}^{-1}$  at  $34\tau_A$  (Figure 4(d)). Similarly, after the second catastrophe, magnetic energy of the system obviously decreases from 1.731 to 1.595 until the prominences obtained the maximum speed (Figure 4(e)), and the magnetic energy inside of the flux rope changes from 0.1338 to 0.05252 at the same time (Figure 4(f)). Furthermore, the corresponding magnetic field configurations are shown in Figure 5. At about  $t = 14\tau_A$ , the flux rope attaches to the surface of the Sun (Figure 5(a)), and then at about  $t = 15\tau_A$ , the prominences form in the inner corona after the first catastrophe (Figure 5(b)). Before the second catastrophe, the prominences already levitate in the inner corona at about  $t = 31\tau_A$  (Figure 5(c)). Due to the second catastrophe, the prominences break out; however, magnetic reconnection does not occur in the two current sheets at about  $t = 32\tau_A$  (Figure 5(d)). Figure 5(e) shows that magnetic reconnection occurs in the vertical and transverse current sheets simultaneously. At about  $t = 34\tau_A$ , the velocity of the CMEs reaches the maximum speed, and the plasmas around the two current sheets are heated by magnetic reconnection (Figure 5(f)).

#### 4. CONCLUSION

Previous work by Zhang et al. (2011) has concentrated on realizing that the physical features in the solar atmosphere, such as temperature and density have important influence on the evolution of the solar eruption event. In this paper, using a 2.5-dimensional MHD simulation, we investigate the role played by the inner coronal null point in the formation and evolution of solar quiescent prominences. We find that magnetic energy of the flux rope system is big when  $\psi_N$  is small. The numerical results show that the bigger  $\psi_N$  usually corresponds to the smaller catastrophic point, and the lower magnetic energy of the flux rope system or inside the flux rope. During the evolution of the flux rope system, while  $\psi_N$  is greater, both the first and second catastrophe occur earlier, but the maximum velocity of CMEs with the erupted prominences is very closer. Thus, we confirm that the catastrophe occurs earlier and more easily when  $\psi_N$  is bigger. However,  $\psi_N$  has little effect on the maximum speed of eruption.

Because there is no inner coronal null point in the dipolar field,  $\psi_N$  is zero. We think that the prominences can be formed not in a dipolar magnetic field, but in a complex magnetic field with the inner coronal null point. Then, we argue that the topological structure with the inner coronal null point is a necessary condition for the formation and evolution of solar quiescent prominences. In a nutshell, it is easier for the prominences to form and to erupt as core parts of the CMEs in the structure with a greater  $\psi_N$ .

The authors are grateful for the anonymous referee's helpful comments on the manuscript. The authors are greatly indebted to Professor J. X. Wang and Professor Y. Q. Hu for valuable advice. The work is supported by the National Natural Science Foundation of China (41174151).

#### REFERENCES

- Antiochos, S. K., Dahlburg, R. B., & Klimchuk, J. A. 1994, *ApJL*, 420, L41  
 Antiochos, S. K., DeVore, C. R., & Klimchuk, J. A. 1999, *ApJ*, 510, 485  
 Anzer, U., & Priest, E. 1985, *SoPh*, 95, 263  
 Athay, R. G., & Illing, R. M. E. 1986, *JGR*, 91, 10961  
 Aulanier, G., & Demoulin, P. 1998, *A&A*, 329, 1125  
 Aulanier, G., & Demoulin, P. 2003, *A&A*, 402, 769  
 Berger, T. E., Liu, W., & Low, B. C. 2012, *ApJL*, 758, L37  
 Bohlin, J. D. 1970, *SoPh*, 13, 153  
 DeVore, C. R., & Antiochos, S. K. 2000, *ApJ*, 539, 954  
 Dryer, M. 1982, *SSRv*, 33, 233  
 Fong, B., Low, B. C., & Fan, Y. 2002, *ApJ*, 571, 987  
 Forbes, T. G., Priest, E. R., & Isenberg, P. A. 1994, *SoPh*, 150, 245  
 Foukal, P. V., & Behr, B. B. 1995, *SoPh*, 156, 293  
 Furth, H. P., Killeen, J., & Rosenbluth, M. N. 1963, *PhFl*, 6, 459  
 Galsgaard, K., & Longbottom, A. W. 1999, *ApJ*, 510, 444  
 Gibson, S. E., Foster, D., Burkepile, J., de Toma, G., & Stanger, A. 2006, *ApJ*, 641, 590  
 Gibson, S. E., Kucera, T. A., Rastawicki, D., et al. 2010, *ApJ*, 724, 1133  
 Gopalswamy, N., Hanaoka, Y., Kundu, M. R., et al. 1997, *ApJ*, 475, 348  
 Gopalswamy, N., & Kundu, M. R. 1990, *SoPh*, 128, 377  
 Habbal, S. R., Druckmüller, M., Morgan, H., et al. 2010, *ApJ*, 719, 1362  
 Heinzel, P., & Anzer, U. 1999, *SoPh*, 184, 103  
 Heinzel, P., Schmieder, B., Fárník, F., et al. 2008, *ApJ*, 686, 1383  
 Heyvaerts, J., Priest, E. R., & Rust, D. M. 1977, *ApJ*, 216, 123  
 Hillier, A., & van Ballegooijen, A. 2013, *ApJ*, 766, 126  
 Hu, Y. Q. 1989, *JCoPh*, 84, 441  
 Hu, Y. Q. 2004, *ApJ*, 607, 1032  
 Hyder, C. L. 1967, *SoPh*, 2, 49  
 Illing, R. M. E. 1984, *ApJ*, 280, 399  
 Illing, R. M. E., & Hundhausen, A. J. 1986, *JGR*, 91, 10951  
 Kippenhahn, R., & Schlüter, A. 1957, *ZA*, 43, 36  
 Kliem, B., Lin, J., Forbes, T. G., Priest, E. R., & Török, T. 2014, *ApJ*, 789, 46  
 Koutchmy, S., Baudin, F., Bocchialini, K., et al. 2004, *A&A*, 420, 709  
 Kuperus, M., & Raadu, M. A. 1974, *A&A*, 31, 189  
 Labrosse, N., Heinzel, P., Vial, J. C., et al. 2010, *SSRv*, 151, 243  
 Li, T., Zhang, J., Zhang, Y. Z., & Yang, S. H. 2011, *ApJ*, 739, 43  
 Litvinenko, Y. E., Chae, J., & Park, S. Y. 2007, *ApJ*, 662, 1302  
 Litvinenko, Y. E., & Wheatland, M. S. 2005, *ApJ*, 630, 587  
 Longcope, D. W., & Forbes, T. G. 2014, *SoPh*, 289, 2091  
 López, A. A., Aulanier, G., Schmieder, B., & Sainz, D. A. 2006, *A&A*, 456, 725  
 Low, B. C. 2001, *JGR*, 106, 25141  
 Low, B. C., Berger, T., Casini, R., & Liu, W. 2012, *ApJ*, 755, 34  
 Low, B. C., & Hundhausen, J. R. 1995, *ApJ*, 443, 818  
 Low, B. C., & Petrie, G. J. D. 2005, *ApJ*, 626, 551  
 Low, B. C., & Zhang, M. 2002, *ApJL*, 564, L53  
 Luna, M., Karpen, J. T., & DeVore, C. R. 2012, *ApJ*, 746, 30  
 Mackay, D. H., Karpen, J. T., Ballester, J. L., Schmieder, B., & Aulanier, G. 2010, *SSRv*, 151, 333  
 Mackay, D. H., & van Ballegooijen, A. A. 2006a, *ApJ*, 641, 577  
 Mackay, D. H., & van Ballegooijen, A. A. 2006b, *ApJ*, 642, 1193  
 MacQueen, R. M., Sime, D. G., & Picat, J. P. 1983, *SoPh*, 83, 103  
 Magara, T. 2012, *ApJ*, 748, 53  
 Marqué, C. 2004, *ApJ*, 602, 1037  
 Martens, P. C., & Zwaan, C. 2001, *ApJ*, 558, 872  
 Martin, S. F. 1998, *SoPh*, 182, 107  
 Milne, A. M., Priest, E. R., & Roberts, B. 1979, *ApJ*, 232, 304  
 Newkirk, G., Jr. 1967, *ARA&A*, 5, 213  
 Okamoto, T. J., Tsuneta, S., Lites, B. W., et al. 2009, *ApJ*, 697, 913  
 Parenti, S. 2014, *LRSP*, 11, 1  
 Petrie, G. J. D., & Low, B. C. 2005, *ApJS*, 159, 288  
 Pneuman, G. W. 1972, *ApJ*, 177, 793  
 Raju, K. P., Desai, J. N., Chandrasekhar, T., & Ashok, N. M. 1993, *MNRAS*, 263, 789  
 Régnier, S., Walsh, R. W., & Alexander, C. E. 2011, *A&A*, 533, L1  
 Saito, K., & Hyder, C. L. 1968, *SoPh*, 5, 61  
 Saito, K., & Tandberg-Hanssen, E. 1973, *SoPh*, 31, 105  
 Schmal, E., & Hildner, E. 1977, *SoPh*, 55, 473  
 Serio, S., Vaiana, G. S., Godoli, G., et al. 1978, *SoPh*, 59, 65  
 Spicer, D. S. 1977, *SoPh*, 53, 305  
 Su, Y., van Ballegooijen, A., & Golub, L. 2010, *ApJ*, 721, 901  
 Tandberg-Hanssen, E. 1995, *The Nature of Solar Prominences* (Dordrecht: Kluwer)  
 Vourlidas, A., Lynch, B. J., Howard, R. A., & Li, Y. 2013, *SoPh*, 284, 179



- Waldmeier, M. 1970, *SoPh*, 15, 167
- Wang, J. X., Zhou, G. P., Wen, Y. Y., et al. 2006, *ChJAA*, 6, 247
- Webb, D. F., Krieger, A. S., & Rust, D. M. 1976, *SoPh*, 48, 159
- Welsch, B. T., DeVore, C. R., & Antiochos, S. K. 2005, *ApJ*, 634, 1395
- Wiik, J. E., Schmieder, B., & Noens, J. C. 1994, *SoPh*, 149, 51
- Xia, C., Chen, P. F., & Keppens, R. 2012, *ApJL*, 748, L26
- Yang, S. H., Zhang, J., Liu, Z., & Xiang, Y. Y. 2014, *ApJL*, 784, L36
- Zhang, J., & Li, L. P. 2009, *RAA*, 9, 1368
- Zhang, Y. Z. 2013, *ApJ*, 777, 52
- Zhang, Y. Z., Feng, X. S., & Song, W. B. 2011, *ApJ*, 728, 21
- Zhang, Y. Z., Hu, Y. Q., & Wang, J. X. 2005, *ApJ*, 626, 1096
- Zhang, Y. Z., & Wang, J. X. 2007, *ApJ*, 663, 592
- Zhang, Y. Z., Wang, J. X., & Hu, Y. Q. 2006, *ApJ*, 641, 572
- Zhou, G. P., Wang, J. X., & Zhang, J. 2006a, *A&A*, 445, 1133
- Zhou, G. P., Wang, J. X., Zhang, J., et al. 2006b, *ApJ*, 651, 1238
- Zirker, J. B. 1989, *SoPh*, 119, 341